J Adv Ceram

Research Article

Ultra-high piezoelectric properties of $BiFeO_3$–$BaTiO_3$ lead-free piezoelectric ceramics enabled by a one-step sintering process

Shiyuan Zhang[1], Xianxin Zhang[1], Jinhao Hu[1], Jinweng Tao[2], Yuanbing Wang[3], Huajun Sun[3], Ali Shoaib[1], Jing-Feng Li[2], Bo-Ping Zhang[1]✉

Cite this article: Zhang S, Zhang X, Hu J, et al. *J Adv Ceram* 2026, **15**(6): 9221302. https://doi.org/10.26599/JAC.2026.9221302

ABSTRACT: $BiFeO_3$–$BaTiO_3$ ceramics have been shown to possess considerable promise in the domain of high-temperature lead-free piezoelectric applications, a property attributable to their elevated Curie temperature and superior piezoelectric properties. However, the inherent issue of high leakage current within this system is a consequence of the unavoidable formation of secondary phases within thermodynamically unstable temperature ranges and the volatility of Bi. This issue severely compromises the high-temperature polarization stability and piezoelectric performance. This high conductance hinders the enhancement of the overall performance and obscures the evolution patterns of intrinsic defects and their influence mechanisms on macroscopic properties, necessitating in-depth investigation. The present study successfully prepared a series of $BiFe_{1+x}O_3$–$BaTiO_3$ ceramics using a one-step sintering process. The Fe content was deliberately designed to exhibit both severe excess and deficiency states. It was found that the Fe non-stoichiometry-induced unique defect evolution behavior. A detailed investigation was conducted to ascertain the influence of the defect configuration on the electrical insulation properties across a range of temperatures and strain levels. The respective contributions of the defect-dipole- and space-charge-induced built-in electric fields to the strain response (before and after polarization) were also examined. It is noteworthy that the pure $0.7BiFeO_3$–$0.3BaTiO_3$ system exhibits remarkable comprehensive properties at room temperature (piezoelectric constant d_{33}^* = 1021 pm/V, strain $S \approx 0.38\%$, and piezoelectric coefficient d_{33} = 201 pC/N). The material exhibits a high Curie temperature of approximately 501 °C, accompanied by a notable high-temperature piezoelectric activity. The peak d_{33} and d_{33}^* values are approximately 380 pC/N (measured at 317.9 °C) and 1481 pm/V (measured at 125 °C), respectively.

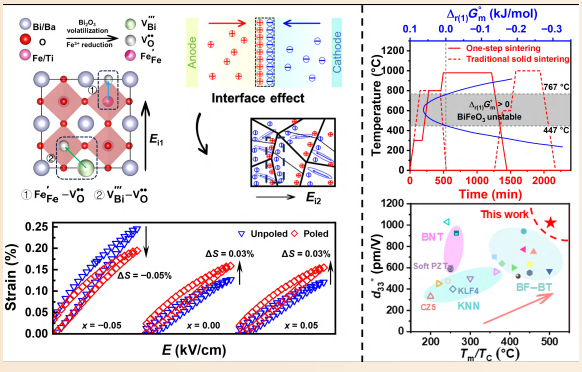

KEYWORDS: $BiFeO_3$–$BaTiO_3$; defect; temperature stability; strain; internal bias field

1 Introduction

The precision displacement actuator market has historically been dominated by traditional lead-based ceramics, which have been recognized for their exceptional piezoelectric properties [1,2]. However, concerns regarding environmental protection and lead toxicity have driven the progressive development of lead-free piezoelectric materials [3,4]. $BiFeO_3$–$BaTiO_3$-based lead-free ceramics have remarkable potential for application due to their combination of good ferroelectric and piezoelectric performances and high Curie temperatures [5,6]. A high piezoelectric constant (d_{33}) of 402 pC/N and a high Curie temperature (T_C) of 454 °C were achieved in ceramics prepared using a water-quenching method with a composition of $0.67Bi_{1.05}Fe_{0.97}Ga_{0.03}O_3$–$0.33BaTiO_3$. This renders them optimal candidates for high-temperature sensing and associated applications, owing to their superior comprehensive performance [7]. However, $BiFeO_3$ exhibits a high Gibbs free energy within the temperature range of 447–767 °C, which renders it prone to phase decomposition and the formation of non-ferroelectric secondary phases, such as the Bi-rich phase $Bi_{25}FeO_{39}$ and/or the Fe-rich phase $Bi_2Fe_4O_9$ [8,9]. Concurrently, during the sintering process, Bi volatilizes, causing local compositional deviations from stoichiometry and exacerbating component segregation within the matrix. The formation of Bi vacancies and alterations in the valence state of Fe^{3+} induce a significant amount of oxygen vacancies in the volatile lattice. The collective effect of these defects is to enhance the hole migration conductivity and ionic mobility, resulting in a decrease in resistivity. This is detrimental to the polarization under external

[1] School of Materials Science and Engineering, University of Science and Technology Beijing, Beijing 100083, China. [2] State Key Laboratory of New Ceramic Materials, School of Materials Science and Engineering, Tsinghua University, Beijing 100084, China. [3] School of Integrated Circuits, Huazhong University of Science and Technology, Wuhan 430074, China.

✉ Corresponding author. E-mail: bpzhang@ustb.edu.cn

Received: January 17, 2026; Revised: March 7, 2026; Accepted: April 21, 2026

electric fields at high temperatures and undermines the enhancement of piezoelectric performance.

To enhance the piezoelectric performance of lead-free ceramics, researchers have adopted various strategies, including phase boundary engineering, domain and/or grain structural optimization, the construction of local structural heterogeneities, and chemical doping [10–13]. In recent years, the application of defect engineering in lead-free piezoelectric systems has garnered particular attention, yielding a series of significant breakthroughs. For instance, in Sr-doped (K,Na)NbO_3 lead-free piezoelectric ceramics, defect dipoles induced by conventional solid-state reaction methods interacted with ferroelectric domain switching, achieving a giant strain of 1.05% and a high signal piezoelectric coefficient (d_{33}^*) of up to 2100 pm/V. The material exhibited a strain output of 0.25% under an electric field of 20 kV/cm, along with fatigue resistance and thermal stability that surpassed those of commercial lead zirconate titanate (PZT) ceramics [14]. Defect engineering has demonstrated considerable research potential in relation to $BiFeO_3$–$BaTiO_3$-based materials [15–17]. It was demonstrated that a "polarization-aging" treatment was capable of achieving oriented arrangements of defect dipoles in $0.67BiFeO_3$–$0.33BaTiO_3$ ceramics. The resultant internal polarization field, when synergistically coupled with depolarization field compensating charges, ultimately yielded a simultaneous high strain of 0.21% and a d_{33}^* of up to 942.05 pm/V [15]. The introduction of Ga^{3+} and A-site Bi vacancies resulted in the establishment of a synergistic transport mechanism of space-charge-limited conduction and electron-limited conduction (SCLC–ELC) [18]. This mechanism enhances the fluctuations of cations deviating from their centers, thereby promoting polarization reversal. Consequently, while preserving a high d_{33} of approximately 205 pC/N, the system demonstrated remarkable thermal stability, with d_{33} values maintained at 310 pC/N ±13% across a substantial temperature range of 100–415 °C [18]. The inherent defects, including Bi vacancies, Fe valence defects, and oxygen vacancies, have been shown to significantly modify the domain structure, conductivity, and polarization behavior of the material [19,20]. This is of particular value in regard to optimizing high-temperature piezoelectric and strain performances [16].

Despite advances in defect engineering across various lead-free systems, the high leakage conductivity of the $BiFeO_3$–$BaTiO_3$ system significantly constrains further exploration of its intrinsic defects [21,22]. Investigating the mechanisms by which defects influence the internal polarization field and high-temperature insulation properties remains challenging. To enhance performance, researchers have expended substantial effort to optimize preparation techniques and introduce modifying elements [23]. Substitution of B-site cations (e.g., Ga^{3+} and Sc^{3+}) has proven effective in suppressing Fe^{3+} valence changes. Sintering in an oxygen atmosphere has also been shown to increase resistivity by an order of magnitude, reaching ranges of 10^{11}–10^{14} Ω·cm [24–28]. Furthermore, optimizing A-site Bi compensation or doping with rare earth elements (e.g., La and Sm) is shown to stabilize the lattice structure, thereby enhancing the ferroelectric and piezoelectric properties of $BiFeO_3$–$BaTiO_3$-based ceramics. The incorporation of sintering additives (e.g., Li_2CO_3 and CuO) is effective in reducing the sintering temperature to below 930 °C, thereby minimizing Bi volatilization and promoting densification processes [29–32]. These strategies for reducing leakage conductivity are usually linked to the prevention of Fe^{3+} valence state changes. However, they do not address composition segregation caused by Bi volatilization and its associated defects, nor can they prevent thermodynamic instability within specific temperature ranges. The potential hazards of $Bi_{25}FeO_{39}$ and/or $Bi_2Fe_4O_9$, therefore, remain unavoidable. Furthermore, adding substances to $BiFeO_3$–$BaTiO_3$ ceramics that are prepared using traditional sintering methods often causes significant relaxation behavior, leading to lower Curie temperatures and poorer piezoelectric properties, making the ceramics exhibit a narrow composition tolerance window.

Recently, Tang *et al.* [33,34] developed a novel, one-step sintering process that has opened new avenues for studying the properties of the $BiFeO_3$–$BaTiO_3$ system, particularly in defect engineering research. This process effectively avoids the thermodynamic instability of $BiFeO_3$ between 447 and 767 °C, not only suppressing the formation of secondary phases such as $Bi_{25}FeO_{39}$ and $Bi_2Fe_4O_9$ but also reducing compositional deviations and oxygen vacancy concentrations caused by bismuth volatilization. Using this novel one-step sintering process, $0.7Bi_{1+x}FeO_3$–$0.3BaTiO_3$ ceramics ($-0.05 \le x \le 0.05$) were synthesized, exhibiting excellent phase stability over a wide range of bismuth non-stoichiometric ratios. Under a 5 kV/cm electric field, their resistivity reached 9.51×10^{10}–4.66×10^{10} Ω·cm, outperforming ceramics prepared by conventional methods. In this study, the $0.7BiFeO_3$–$0.3BaTiO_3$ ceramics prepared by the one-step sintering method were confirmed by X-ray diffraction (XRD) refinement to possess a stable coexistence of rhombohedral and pseudocubic (R/PC) phases (~50%/50%), demonstrating that this composition lies within the morphotropic phase boundary (MPB) region. Therefore, selecting this system as the baseline composition for investigating the regulation of defect evolution and electrical properties by Fe non-stoichiometry is fully justified. Accordingly, we successfully synthesized $0.7BiFe_{1+x}O_3$–$0.3BaTiO_3$ (abbreviated as BF_{1+x}–30BT) ceramics with x ranging from −0.05 to 0.05 via a one-step preparation method, where negative and positive values represent Fe deficiency and Fe excess, respectively. The Fe content was deliberately designed to vary across a broad range, from severe deficiency to severe excess, amplifying defect effects and structural variations. The obtained samples exhibited high structural and piezoelectric stability, along with high bulk resistivity, across a wide composition window, providing ideal research samples for elucidating the mechanism of intrinsic defects and further enhancing the material's comprehensive performance. Further characterization employing multiple techniques—including XRD, piezoelectric–electric (P–E), dielectric constant (ε_r)–T curves, energy dispersive spectroscopy (EDS), and piezoelectric force microscopy (PFM). This systematic investigation into the construction of internal electric fields by space charges and defect dipoles within the $BiFeO_3$–$BaTiO_3$ system, along with their synergistic contribution to macroscopic strain behavior, provides new research perspectives and experimental evidence for designing high-performance, lead-free piezoelectric ceramics through precise defect engineering.

2 Experimental

A series of $0.7BiFe_{1+x}O_3$–$0.3BaTiO_3$ (x = −0.05, −0.03, −0.01, 0, 0.01, 0.03, and 0.05) ceramics were prepared using a one-step sintering process. Highly pure raw materials, including α-Bi_2O_3 (99%, Aladdin), Fe_2O_3 (99%, Xilong Scientific), and nano-$BaTiO_3$ (99.9%, Aladdin), were weighed and wet-milled at 250 r/min for 16 h using a planetary ball mill with anhydrous ethanol. After drying in an oven at 80 °C for 8 h, 2 wt% polyvinyl alcohol (PVA) was added to the powders. The mixture was then pressed into ϕ10 mm × 1 mm disks at 100 MPa. The PVA was removed by heating at 300 °C for 2 h. The samples were kept at 800 °C for 3 h and then sintered at 970 °C for 12 h. After polishing the top and bottom surfaces of the ceramics, silver electrodes were pasted and

fired at 600 °C for 0.5 h. The ceramics were polled by using a direct-current electric field of 4 kV/cm at 100 °C for 0.5 h in a silicone oil bath.

The phase composition of the sintered ceramics was detected by an X-ray diffractometer (D/max-RB, Rigaku Inc., Japan) with Cu Kα radiation (λ = 1.5418 Å). The phase fractions and lattice parameters were determined using the Rietveld refinement program (General Structure Analysis System). The density was evaluated using Archimedes' method. A field emission scanning electron microscope (FESEM; SUPRATM55, Carl Zeiss, Japan) was employed to examine the fracture microstructure, while energy-dispersive X-ray spectroscopy (EDS) and elemental mapping were performed on the ceramics. The microscopic domain structure was observed using a piezoresponse force microscope (PFM; MFP-3D, Oxford Instruments, USA). The local piezoelectric response of the ceramics was detected by switching spectroscopy piezoresponse force microscopy (SS-PFM). The chemical states of the ceramic components were characterized by an X-ray photoelectron spectrometer (XPS; PHI-5300, PHI, USA) using Al Kα radiation ($h\nu$ = 1486.6 eV) as the X-ray source.

The planar electromechanical coupling coefficient (k_p) was determined using the resonance–antiresonance method with an Agilent 4294A precision impedance analyzer. Polarization–electric (P–E) hysteresis loops, current–electric (I–E) loops, and strain loops (S–E) were generated using a ferroelectric tester (TF Analyzer 1000, aixACCT Systems, Germany), and the corresponding remnant polarization (P_r), maximum polarization (P_m), coercive field (E_c), and maximum current (I_m) were summarized. Leakage current density and resistivity were measured using a ferroelectric tester (RT6000HVA, Radiant Technologies, Inc., USA). Temperature-dependent dielectric spectra and impedance spectra were obtained using a precision impedance analyzer (Agilent 4294A, Hewlett–Packard, USA). The piezoelectric properties were characterized by a quasi-static piezoelectric coefficient d_{33} tester (ZJ-3A, Institute of Acoustics, Chinese Academy of Sciences, China).

3 Results and discussion

Figure 1(a) illustrates the comparison of $BiFeO_3$–$BaTiO_3$-based ceramics, which were prepared using traditional solid sintering and a one-step sintering process in this study, in terms of their d_{33} and d_{33}^*. The BF_{1+x}–30BT ceramics prepared using the one-step sintering process demonstrate exceptional overall performance, achieving a high d_{33} of up to 201 pC/N and an ultrahigh d_{33}^* of up to 1021 pm/V at a composition of $0.7BiFeO_3$–$0.3BaTiO_3$. This combination of performance characteristics surpasses that of most piezoelectric BF–BT ceramic systems [15,35–43] while demonstrating stable performance across a wide range of off-stoichiometric ceramics, including cases of Fe deficiency or excess. In contrast, ceramics prepared using traditional solid sintering typically rely on quenching or poling processes to enhance d_{33} or d_{33}^*, although achieving significant improvements in both remains a major challenge. Notably, the ceramic exhibits excellent piezoelectric properties and a Curie temperature as high as T_C = 503 °C, surpassing extensively studied lead-free piezoelectric systems such as sodium potassium niobate $(K_{0.5}Na_{0.5})NbO_3$ [44–49] and $(Bi_{0.5}Na_{0.5})TiO_3$ [50–52] (Fig. 1(b)). This makes the material highly competitive in the field of high-temperature piezoelectric ceramics, including those containing lead [47].

Figure 1(c) shows a flowchart that compares the one-step sintering process with traditional solid sintering. In this method,

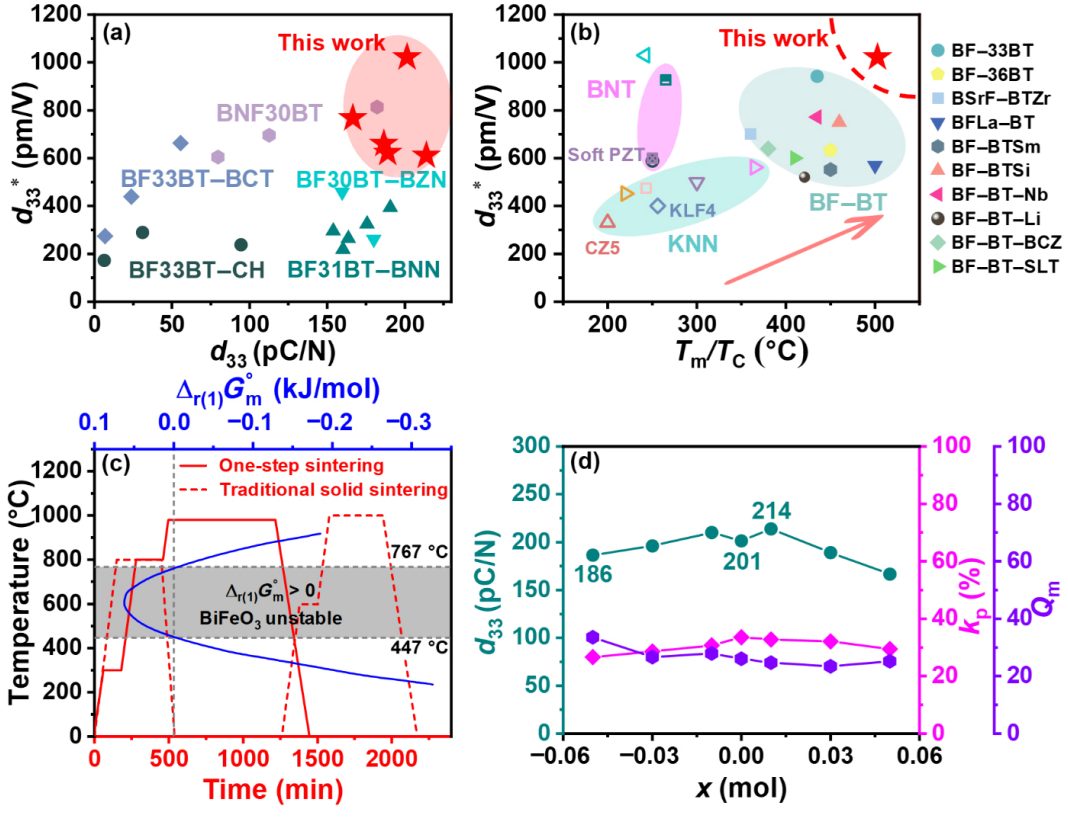

Fig. 1 (a) Comparison of d_{33} and d_{33}^* between BF_{1+x}–30BT ceramics synthesized by traditional preparation process and one-step sintering process; (b) comparison of T_C and d_{33}^* between one-step sintering process $BiFeO_3$–$BaTiO_3$ and other ceramics for optimizing comprehensive performance; (c) schematic diagram of one-step sintering process and conventional solid-phase sintering process; (d) x-dependence of d_{33}, k_p, and Q_m.

$BaTiO_3$ replaces the traditional raw materials $BaCO_3$ and TiO_2. This effectively integrates the separate thermal treatment steps required for traditional solid-state sintering—namely, debinding, calcination, and sintering—into a single process, thereby greatly improving preparation efficiency. Thermodynamic analysis based on Gibbs free energy for $BiFeO_3$, $Bi_2Fe_4O_9$, and $Bi_{25}FeO_{39}$ indicates that the method bypasses the thermodynamically unstable region of $BiFeO_3$, thereby effectively suppressing the formation of the impurities $Bi_2Fe_4O_9$ and $Bi_{25}FeO_{39}$ during the heat treatment process. This contributes to stable piezoelectric performance, as shown in Fig. 1(d), where $d_{33} \geq 186$ pC/N is observed across a wide compositional range of $-0.05 \leq x \leq 0.03$. The highest piezoelectric responses, $d_{33} = 214$ pC/N and $d_{33} = 210$ pC/N, are observed when $x = \pm 0.01$. Furthermore, BF_{1+x}–30BT ceramics prepared using this method demonstrate stability in their electromechanical coupling coefficient (k_p) and mechanical quality factor (Q_m), with values of approximately 0.3 and 30, respectively, thereby confirming the reliability of the process.

Figure 2 shows the SEM images of the fracture morphology for the BF_{1+x}–30BT ceramics prepared using the one-step sintering process, alongside their respective relative densities and average grain sizes. All ceramics exhibit clear grain boundaries and a dense microstructure, with relative densities exceeding 90%. Within the range of $-0.05 \leq x \leq -0.01$, the average grain size of BF_{1+x}–30BT ceramics remains relatively constant at approximately 8.2 μm. However, within the range of $0 \leq x \leq 0.05$, the grain size continuously decreases as the value of x increases, yielding measured values of 8.67, 8.52, 6.5, and 5.7 μm. The refined grains are attributed to the high melting point of Fe_2O_3 (1565 °C), which inhibits grain growth during sintering. Figure S1 in the Electronic Supplementary Material (ESM) shows that the elemental distribution maps of the polished surface of the BF_{1+x}–30BT ceramics reveal a uniform distribution of all elements. No elemental segregation or formation of a core–shell structure was observed. This phenomenon is independent of the x value. These findings confirm the feasibility of the one-step sintering process for such complex compositions.

Figure 3 shows the XRD patterns of the BF_{1+x}–30BT ceramics, alongside their phase fractions and lattice parameters. All ceramics exhibit a perovskite structure and highly similar XRD patterns within the range of $-0.05 \leq x \leq 0.05$, indicating good structural stability of the BF_{1+x}–30BT ceramics prepared by the one-step sintering process. However, as illustrated in Fig. 3(b), impurity peaks were observed within the range of 27.89°–27.99° for ceramics with $x = -0.05$ and -0.03. These peak positions correspond to the characteristic peaks of non-ferroelectric β-Bi_2O_3, which originates from an excess of α-Bi_2O_3 in the raw materials and transforms into relatively inert β-Bi_2O_3 during subsequent thermal processing. Compared with harmful phases rich in Bi ($Bi_{25}FeO_{39}$) and Fe ($Bi_2Fe_4O_9$), leading to local compositional deviations from the intended values, the formation of this β-Bi_2O_3 contributes to the stable piezoelectric performance of BF_{1+x}–30BT ceramics. Furthermore, this indicates that the volatilization of Bi has been adequately compensated by the excess amount of raw material, which helps to reduce the defect content. The corresponding solid-state reaction can be described as Reaction (1):

$$\alpha\text{-}Bi_2O_3 + Fe_2O_3 + BaTiO_3 \rightarrow BF\text{-}x BT + \beta\text{-}Bi_2O_3 \quad (1)$$

In traditional solid sintering, the excessive volatilization of Bi has been observed to result in the formation of $Bi_{25}FeO_{39}$ or $Bi_2Fe_4O_9$. These secondary phases emerge from unstable temperature regions during the sintering process and compositional segregation, which leads to local compositional inhomogeneities. Furthermore, our preliminary research, which is

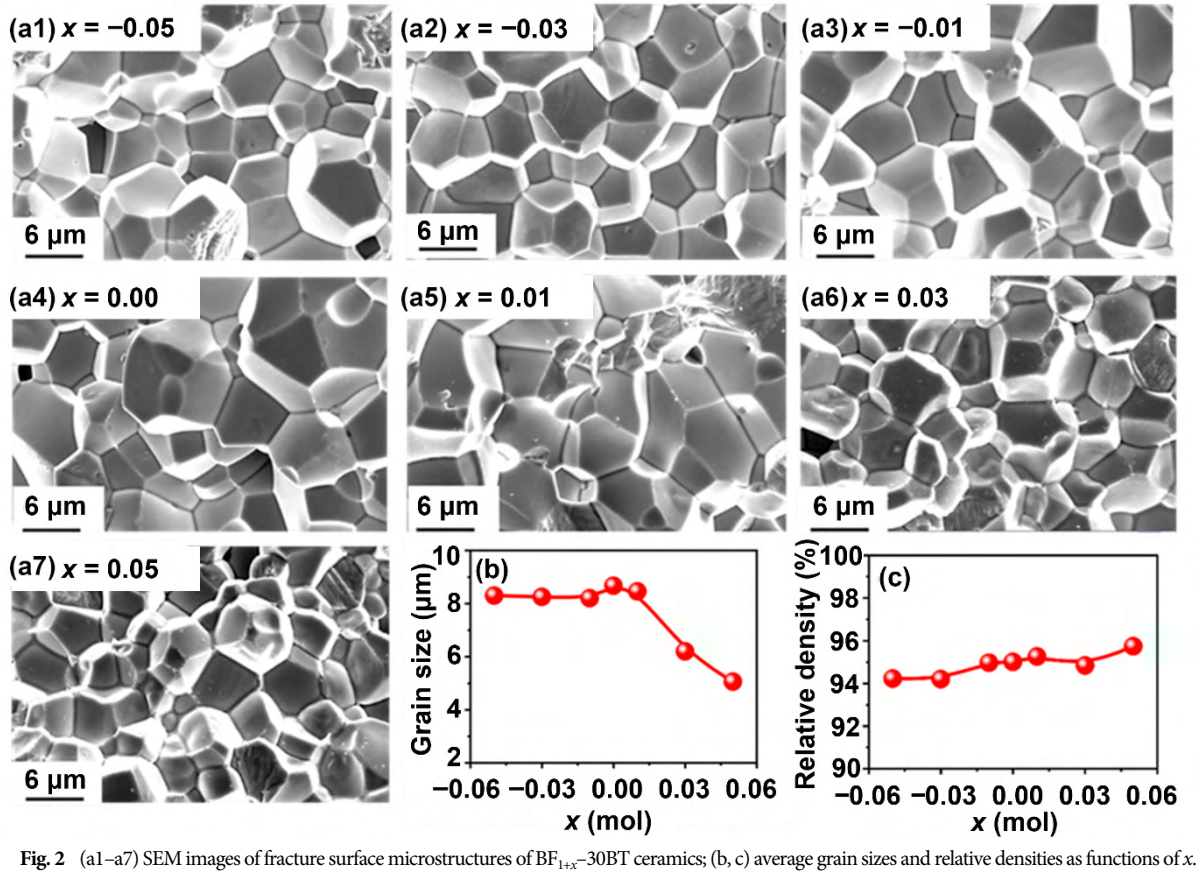

Fig. 2 (a1–a7) SEM images of fracture surface microstructures of BF_{1+x}–30BT ceramics; (b, c) average grain sizes and relative densities as functions of x.

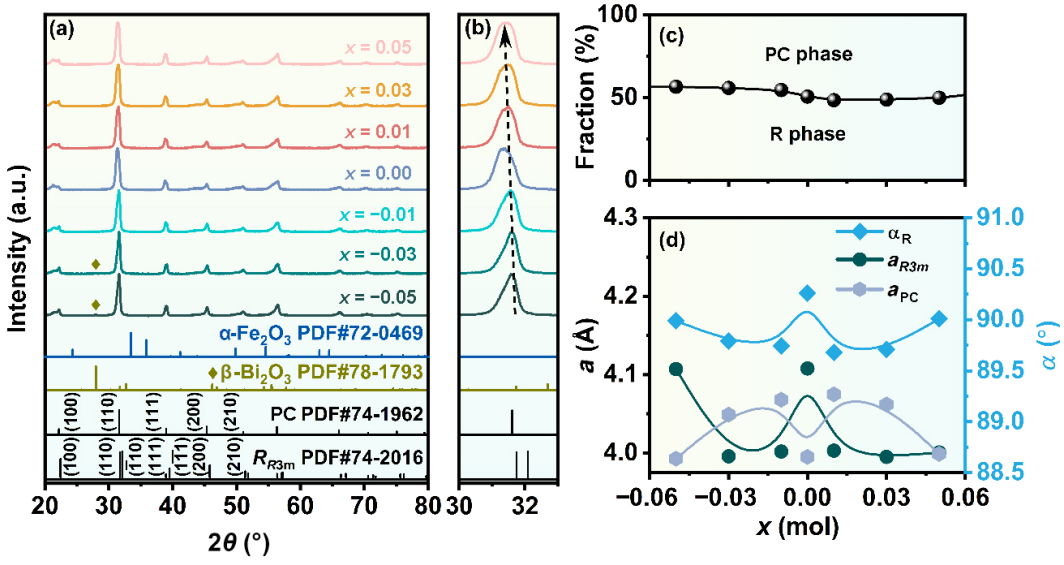

Fig. 3 (a, b) XRD patterns of BF_{1+x}–30BT ceramics; (c, d) phase fraction and lattice parameter of R and PC phases of BF_{1+x}–30BT ceramics.

yet to be published, indicates that excess Fe_2O_3 persists as a secondary phase within the $BF_{1.03/1.05}$–25BT system. However, no traces of Fe_2O_3 were detected in the BF_{1+x}–30BT ceramics studied herein, indicating that Fe_2O_3 has achieved an effective solid solution within the $BiFeO_3$–$BaTiO_3$ matrix. This discrepancy is attributable to the comparatively low $BiFeO_3$ content in the BF_{1+x}–30BT system.

The width of the main diffraction peak (110) near 31° and the splitting of the (111) diffraction peak at approximately 39° collectively indicate that all ceramics exhibit the coexistence of rhombohedral (R, *R*3*m*) and pseudocubic (PC, $Pm\bar{3}m$) phases. As the value of x increases, the (110) diffraction peak undergoes a gradual shift toward lower angles and broadens (Fig. 3(b)), which is attributable to alterations in phase ratios or lattice contraction. It is noteworthy that when $x = 0$, the diffraction peaks, including the (110) main peak, deviate from the trend line, shifting toward lower angles. A sophisticated analysis employing GSAS software (Fig. S2 and Table S1 in the ESM) suggests that the composition ratio of R phase to PC phase (C_R/C_{PC}) exhibits a slight decrease as x increases. The C_R/C_{PC} ratio is approximately 54.5 : 45.5, 56.4 : 43.6, 48.3 : 51.7, and 50.6 : 49.4 for $x = -0.05$, -0.01, 0.00, and 0.05, respectively, and remains stable at approximately 50%. Such structural stability proves exceptionally difficult to achieve under off-stoichiometric ceramics. The one-step sintering process effectively suppresses the formation of harmful secondary phases and stabilizes the main phase composition. This consequently ensures a relatively stable C_R/C_{PC} ratio in the BF_{1+x}–30BT ceramics. Establishing an appropriate C_R/C_{PC} ratio constitutes an effective strategy for reducing the domain reversal barrier, which is widely recognized as a key factor in achieving a high electrical response d_{33} [53,54]. Furthermore, analysis of the lattice parameters indicates that the ceramic with $x = 0$ exhibits the largest rhombohedral cell parameter a_{R3m} and the largest axial angle α, as well as the smallest pseudocubic cell parameter a_{PC}. This is indicative of greater lattice mismatch and significant lattice distortion. Off-stoichiometric ceramics have been shown to exhibit enhanced stability in terms of lattice parameters (a_{R3m}/a_{PC} and α), indicating reduced lattice distortion. Considering their stable phase proportions and variations relative to the matrix element ratio, this reduction in lattice distortion may be associated with the suppression of defect formation caused by both Fe deficiency and excess.

Figure 4 shows the dielectric properties of BF_{1+x}–30BT ceramics, which exhibit pronounced dielectric peaks in the vicinity of T_C. Within the frequency range of 1–1000 kHz, the dielectric constant ε_r decreases with increasing frequency, while the dielectric peak broadens and shifts toward higher temperatures, as shown in Fig. 4(a). It is noteworthy that the ceramics with Fe deficiency ($-0.05 \le x < 0$) and Fe excess ($0 < x \le 0.05$) exhibit distinct relaxation behaviors. The ceramics with $-0.05 \le x < 0$ exhibit pronounced frequency dispersion specifically at the low frequency of 1 kHz (Figs. 4(a1)–4(a3)), indicating that high concentrations of defects and/or defect dipoles may induce space charge effects. Conversely, within the Fe-excess region, the frequency dispersion effect diminishes with increasing x, while the characteristics of the diffuse phase transition become more pronounced (Figs. 4(a4)–4(a7)). This phenomenon is associated with grain refinement, whereby the disruption of the long-range order of ferroelectric domains induces stronger relaxation properties. The diffusion coefficient γ, calculated based on the modified Curie–Weiss law (Fig. 4(b)), further corroborates this transition. At $x = -0.01$, the value of γ is approximately 1.12, indicating near-normal ferroelectricity, whereas as x increases from 0 to 0.05, γ ascends from 1.34 to 1.81. The T_C value remained stable at approximately 500 °C for all ceramics, further validating the stability of the phase structure. This is of crucial importance for maintaining a high piezoelectric response d_{33} while facilitating a continuous transition of ferroelectricity to relaxation properties driven by grain refinement. Nevertheless, these findings do not fully account for the dual dependence of frequency dispersion on both Fe deficiency and excess in this system. Consequently, a thorough investigation into the intrinsic mechanisms by which the internal defect state of the ceramic affects this behavior is needed.

It is well known that the high-temperature sintering process for $BiFeO_3$-based ceramics induces the formation of Bi vacancies, designated V_{Bi}''', due to the volatilization of Bi_2O_3. To maintain charge balance, this process drives the reduction of some Fe^{3+} to Fe^{2+}. This phenomenon is evidenced by a negative shift in binding energy, concomitant with the formation of oxygen vacancies, denoted by $V_O^{\cdot\cdot}$. Consequently, $BiFeO_3$–$BaTiO_3$ ceramics exhibit multiple defects, including V_{Bi}''', Fe_{Fe}', and $V_O^{\cdot\cdot}$, as illustrated in Fig. 5(a). The defect reactions shown in Reactions (2)–(4):

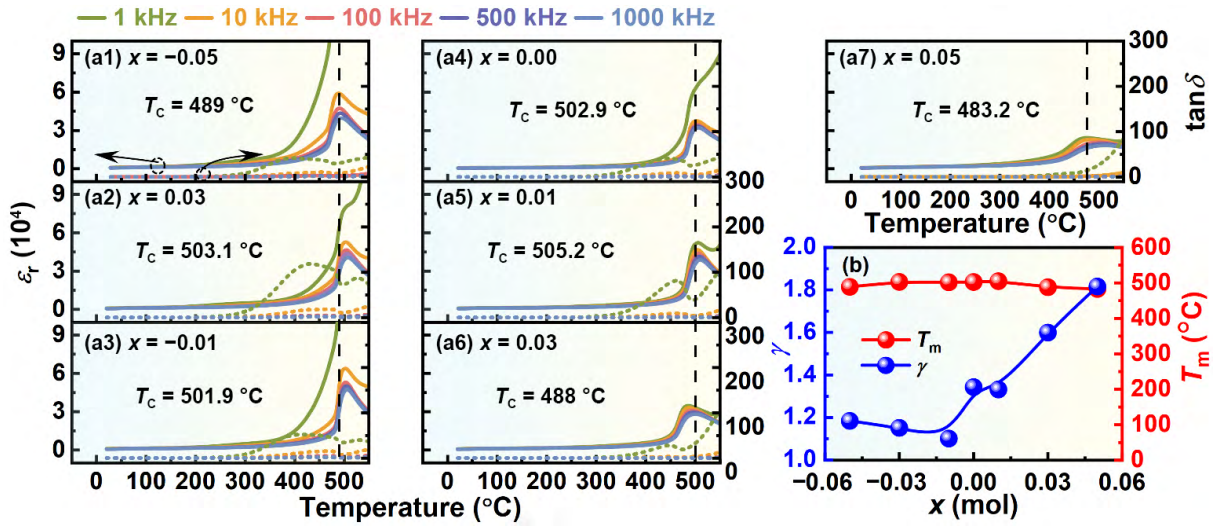

Fig. 4 (a1–a7) ε_r–T and tanδ–T curves for BF_{1+x}–30BT ceramics at 1–1000 kHz frequencies. (b) γ and T_C as a function of x.

$$2BiFeO_3 \rightarrow Bi_2O_3 \uparrow + 2Fe_{Fe}^{\times} + 2V_{Bi}^{'''} + 3V_O^{\cdot\cdot} + 3O_O^{\times} \quad (2)$$

$$2Fe_{Fe}^{\times} + O_O^{\times} \rightarrow \frac{1}{2}O_2 \uparrow + 2Fe_{Fe}^{'} + V_O^{\cdot\cdot} \quad (3)$$

$$2V_O^{\cdot\cdot} + O_2 \rightarrow 2O_O^{\times} + 4h^{\cdot} \quad (4)$$

The oppositely charged defects either freeze gradually during the cooling process or form defect dipoles, thereby generating an internal polarization field (E_i). The variation in defect concentration with x was analyzed semiquantitatively via XPS testing. The presence of both Fe^{2+} and Fe^{3+} ions in the ceramics was confirmed by the broad and asymmetrical XPS spectra of Fe 2p electrons. The fitted XPS spectra for the Fe 2p, Bi 4f, and O 1s peaks are presented in Fig. 5(c) and Fig. S3 in the ESM, respectively. By integrating the peak areas following the deconvolution process, the variations in the concentrations of Fe^{2+} and Bi^{3+} were determined. Due to Bi^{3+} volatilization, off-stoichiometric Bi (or Fe) and the formation of β-Bi_2O_3, which are the parameters affecting the Bi^{3+} content, the ratio of $Bi^{3+}/(Fe^{2+} + Fe^{3+})$ increases initially and then decreases with increasing x. The Fe^{3+}/Fe^{2+} ratio is 61% : 39%, 62% : 38%, and 67% : 33% when x varies from −0.05 to 0.05, respectively, caused by the reduction of some Fe^{3+} to Fe^{2+}. Therefore, it can be inferred that the $Fe_{Fe}^{'}$ and $V_{Bi}^{'''}$ defects follow the trend of the dotted line in Fig. 5(c) as x increases: The $Fe_{Fe}^{'}$ defects decrease monotonically, and the $V_{Bi}^{'''}$ vacancies initially decrease and then increase. The x = 0 ceramic should have the lowest content of multiple defects, thereby showing the lowest leakage current density (J) value of 1.3×10^{-8} A/cm² alongside a relatively high resistance ρ = 3.83×10^{11} Ω·cm (Figs. 5(d) and 5(e)). As shown in the inset, the low J value of BF_{1+x}–30BT ranges from 10^{-7} to 10^{-8} A/cm², indicating that the one-step sintering process effectively avoids the performance degradation caused by impurity phases and defects. Due to the low defect concentration, the x = 0 ceramic exhibits low ε_r and tanδ values in the frequency range from 1 kHz to 1 MHz. As the frequency increases, the space charge polarization effects caused by the defects gradually diminish [55]. This results in the ε_r and tanδ values of all ceramics approaching uniformity. Following polarization, resonance peaks induced by domain reorientation and defect dipoles can be observed within the 10^5–10^6 Hz frequency range, as illustrated in Fig. S4 in the ESM.

Figures 5(g) and 5(h) show the ferroelectric properties of the ceramics in their unpolarized and polarized states. As the external electric field E_{ext} increased, all ceramics exhibited sharp current peaks and saturated P–E curves, which are characteristic features of ferroelectric materials (Fig. S5 in the ESM). Polarization increased the maximum P_m and remanent polarization P_r values to 36.2–43.9 and 28.2–34.6 μC/cm², respectively, due to the greater degree of domain switching. All the ceramics exhibited robust piezoelectric responses. This P_m/P_r stability is due to the stable phase ratio of C_R/C_{PC} within the suitable range of 48.3 : 51.7 to 56.4 : 43.6. Notably, the x = 0 ceramic exhibited a more rectangular shape after polarization than the other ceramics, indicating a substantial coercive field E_C. Additionally, as shown in Fig. 5(h), the x-dependent E_i calculated using the equation $E_i = |E_C^+ + E_C^-|/2$ exhibited distinct trends before and after polarization (E_C^+ and E_C^- represent the positive and negative coercive fields, respectively). Before polarization, the ceramics with $-0.05 \le x < 0$ showed notable E_i values of approximately 0.39, 0.46, and 0.63 kV/cm under external fields of 40, 50, and 60 kV/cm, respectively, due to their high defect content and the formation of defect dipoles. These effects diminished as x increased. Conversely, an unusually high E_i value of approximately 3.23 kV/cm was observed in the highly insulating x = 0 ceramic after polarization, despite an external field of only 40 kV/cm. This high E_i value cannot be explained solely by the defect dipole mechanism. The macroscopic polarization drives the motion of free charges [18,56]. These free charges induce an internal bias field E_{i2} parallel to the polarization direction due to interface effects (Fig. 5(f)) [57].

Figure 6(a) presents the high-temperature impedance spectra of three typical ceramics with x = −0.05, 0, and 0.05. The complete spectra at temperatures ranging from 320 to 480 °C, with an increment of 40 °C, are presented in Fig. S6 in the ESM, indicating a well-defined semicircular for all ceramics. Due to the decrease in the carrier concentration as x increases, the total resistivity (R_{tot}) shows an upward trend within the 320–400 °C temperature range (Fig. 6(b)). As the temperature is increased beyond 400 °C, the decreasing trend of R_{tot} with temperature diminishes, and no significant variations are observed at different x values. This finding suggests that the impact of carrier concentration on the conductance behavior diminishes, and the additional factors gradually dominate the conduction process. The activation energy (E_a) calculated using the Arrhenius equation is illustrated in Fig. 6(c) [38].

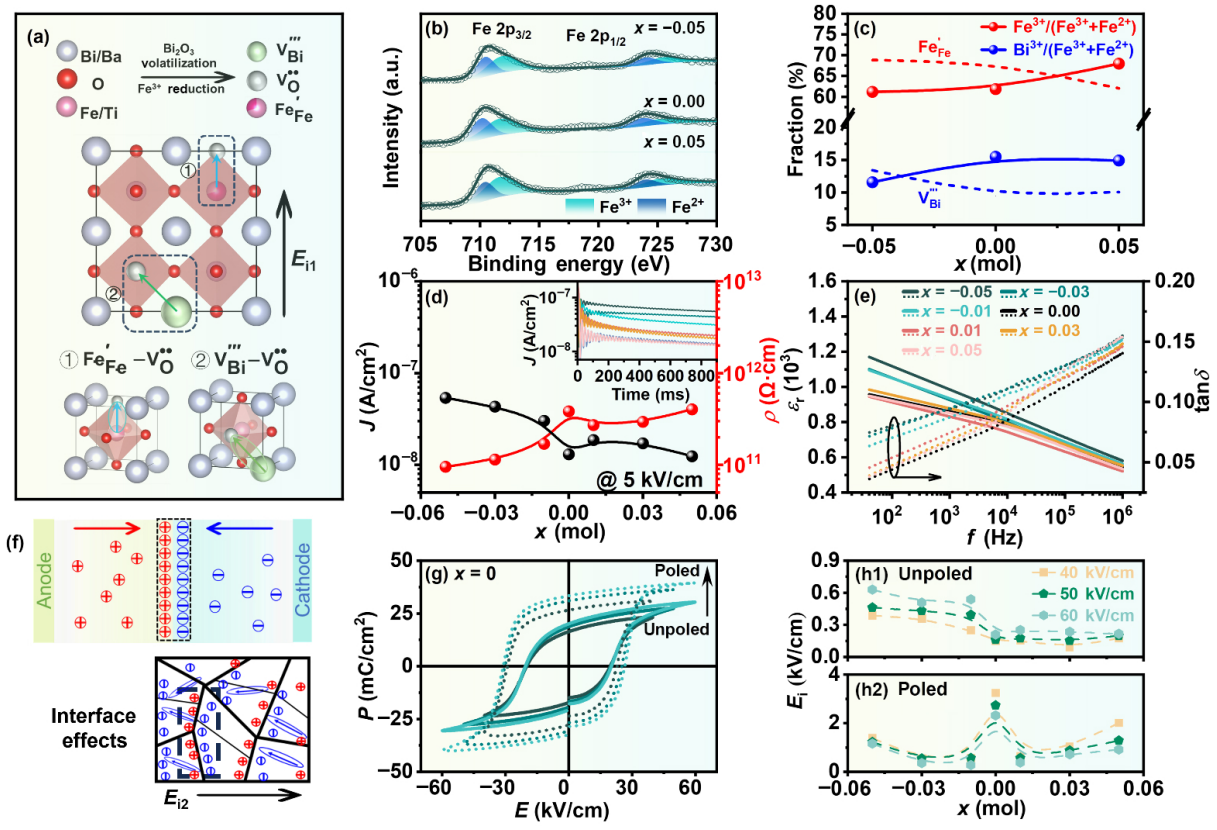

Fig. 5 (a) Schematic diagram of defect formation in $BiFeO_3$–$BaTiO_3$; (b) XPS spectra and peak fitting results of Fe 2p; (c) relative percentages of Fe^{3+} and Bi^{3+}, along with corresponding trends in defect evolution; (d) leakage current density J and resistance ρ of BF_{1+x}–30BT at room temperature (RT); (e) ε_r–f and tanδ–f curves of BF_{1+x}–30BT ceramics at RT; (f) interface effects of poled $BiFeO_3$–$BaTiO_3$ ceramics induced by depolarization fields; (g) P–E loops of unpoled and poled BF–30BT (x = 0) ceramic at 40, 50, and 60 kV/cm; and (h1, h2) E_i of unpoled and poled BF_{1+x}–30BT piezoelectric ceramics at 40, 50, and 60 kV/cm.

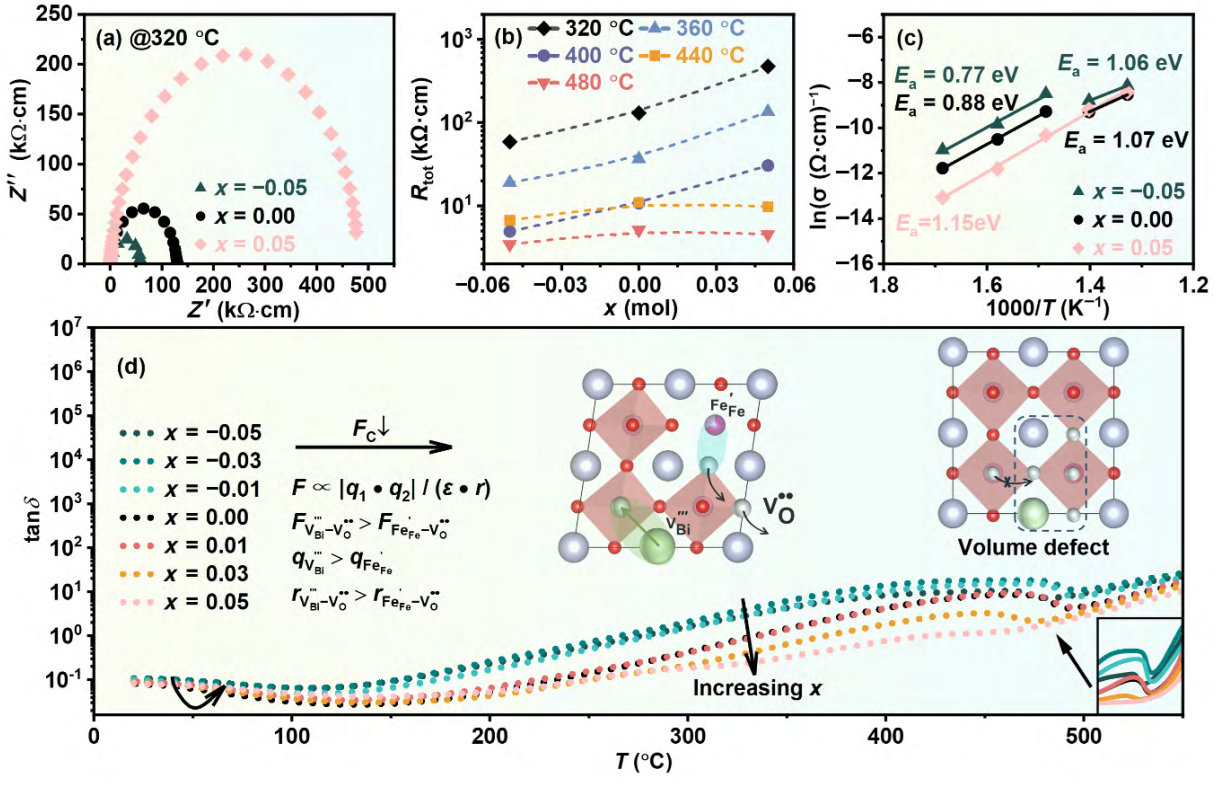

Fig. 6 (a) Impedance spectra of BF_{1+x}–30BT ceramics at 320 °C: x = −0.05, 0, and 0.05; (b) R_{tot} of BF_{1+x}–30BT ceramics from 320 to 480 °C; (c) Arrhenius plot of BF_{1+x}–30BT ceramics; and (d) tanδ–T curves measured at 10 kHz of BF_{1+x}–30BT ceramics.

$$\sigma = \frac{l}{RS} \tag{5}$$

$$\sigma = \sigma_0 \exp\left(\frac{E_a}{K_B T}\right) \tag{6}$$

where σ is the electrical conductivity; l is the sample length; R is the resistance; S is the area; σ_0 is the pre-exponential factor; E_a is the activation energy; k_B is the Boltzmann constant; T is the absolute temperature. Within the 320–400 °C range, the E_a values are recorded as 0.77, 0.88, and 1.15 eV, respectively, aligning with the typical activation energy for oxygen vacancy migration. The higher energy barrier for oxygen vacancy migration in ceramics explains their improved insulating properties as x increases, which help mitigate high-temperature conduction losses. As the temperature rises to 440–480 °C, the activation energy values for the x = 0 and −0.05 ceramics increase to 1.06 and 1.07 eV, respectively, approaching the stable values observed in ceramic with x = 0.05. This suggests that the predominant mechanism governing electrical conductivity undergoes a transition from being exclusively governed by the oxygen vacancy concentration to being influenced by thermal activation. These trends of R_{tot} and E_a with increasing temperature are consistent with the observed behavior of tanδ, as illustrated in Fig. 6(d). Analysis of the variation in tanδ with temperature provides insights into the underlying mechanism of defect and structure evolution.

As the temperature of the ceramics is increased from room temperature to 200 °C during the heating process, the growth of tanδ for all ceramics occurs relatively slowly. In this stage, the tanδ of BF_{1+x}–30BT ceramics demonstrates a dependence on oxygen vacancy concentration, with the x = 0 composition exhibiting a lower tanδ due to its lower oxygen vacancy concentration. Within this temperature range, the conductive behavior of the ceramic is primarily dominated by hole carriers. As the temperature rises further, the tanδ of all ceramics rises significantly. This change is primarily attributed to two factors: (1) Thermal excitation of hole carriers leads to an increase in their mobility, and (2) oxygen vacancies become thermally activated and serve as the main charge carriers. Notably, the binding effect of defect dipoles on oxygen vacancies begins to manifest at this stage. They "pin" the oxygen vacancies in local positions through electrostatic interactions, allowing only those oxygen vacancies that acquire sufficient energy to overcome the binding and participate in migration or conduction processes. In the temperature range of 300 °C and above, ceramics with high concentrations of Fe'_{Fe} defects (−0.05 ≤ x < 0) exhibit elevated tanδ values and identifiable loss peaks [58]. Conversely, ceramics exhibiting reduced Fe'_{Fe} defect concentrations (0 < x ≤ 0.05) demonstrate a conspicuously diminished tanδ, with the peak approaching complete extinction at approximately 400 °C when x = 0.05. The ceramics at x = 0 exhibit intermediate behavior between the two. Within this temperature range, the migration of oxygen vacancies becomes the dominant mechanism for leakage conduction loss, relying on the "hopping" diffusion of oxygen ions to adjacent oxygen vacancies. This mechanism directly manifests as a sharp increase in tanδ under low-frequency conditions (Fig. 4). The ease with which oxygen vacancies can achieve such "hopping" diffusion is directly constrained by the binding strength of defect dipoles to them, specifically the dissociation ability of the defect dipoles. In comparison with V'''_{Bi} defects, the Coulomb interaction (F_C) between Fe'_{Fe} and $V^{\cdot\cdot}_O$ defects is weaker, thus rendering the $Fe'_{Fe}-V^{\cdot\cdot}_O$ defect dipoles more susceptible to thermal dissociation than $V'''_{Bi}-V^{\cdot\cdot}_O$, consequently releasing a greater number of mobile oxygen vacancies. The E_a measured in the temperature range of 300–420 °C increases with the value of x, further confirming this change. Based on the impedance spectroscopy data, the leakage current density at various temperatures was calculated for each composition, as shown in Fig. S6(d) in the ESM. The results reveal that the x = 0.05 ceramic exhibits the lowest leakage current across the measured temperature range. As x increases, the leakage current decreases at elevated temperatures, indicating enhanced high-temperature insulation. This trend correlates well with the increased activation energy E_a and the suppressed tanδ, confirming that the enhanced electrostatic interaction between charged defects effectively restricts oxygen vacancy migration.

As the temperature rises further, reaching approximately 400 °C, the growth trend of tanδ for all ceramics slows down, and a distinct dielectric peak is formed. This behavior is consistent with the phenomenon where the total R_{tot} tends to stabilize or is suppressed, accompanied by an observable increase in E_a. This outcome is partly attributable to the decrease in mobility that arises from the enhanced symmetry of the crystal structure, which limits the migration pathways of oxygen vacancies. Furthermore, the local ordered structures formed by high-density defect clusters (e.g., volume defects) contribute to the pinning effect on oxygen vacancy migration. Xue *et al.* [58] found that near the T_C, as the temperature increases, the carrier concentration increases, while the mobility decreases significantly. This behavior indicates that the contribution of oxygen vacancy migration to electrical conductivity diminishes with rising temperature, and thermally activated electronic conduction becomes increasingly dominant at high temperatures. This conclusion is consistent with the activation energy trend extracted from impedance spectroscopy (Fig. 6(c)), reflecting enhanced restriction of oxygen vacancy migration. Upon attaining the temperature T_C, the tanδ values of all ceramics demonstrate a pronounced increase, chiefly attributable to the substantial kinetic resistance experienced by polarization fluctuations and reversals within the critical region of the ferroelectric–paraelectric phase transition.

As illustrated in Fig. 7(a), the bipolar strain curves of BF_{1+x}–30BT ceramics are shown before and after polarization. Prior to polarization, the bipolar strain curve manifests a characteristic "butterfly" shape, with the asymmetry being most pronounced at x = −0.05 and gradually weakening as the value of x increases. When x = 0, the curve approaches symmetry, and this symmetrical characteristic is largely maintained in the range of −0.05 ≤ x < 0. The observed asymmetry in the strain curve is attributed to the internal electric field (E_{i1}) within the material, which is closely related to the presence of two types of charged defects: $\left[Fe'_{Fe}-V^{\cdot\cdot}_O\right]^{\cdot}$ and $[V'''_{Bi}-V^{\cdot\cdot}_O]'$ [15,59]. Research has demonstrated that defect dipoles with a net zero charge are capable of inducing the internal bias electric field E_{i1} with greater efficacy [60]. In the context of ceramics with −0.05 ≤ x < 0, it has been observed that the nonzero net charge defects, $\left[Fe'_{Fe}-V^{\cdot\cdot}_O\right]^{\cdot}$ and $[V'''_{Bi}-V^{\cdot\cdot}_O]'$, exhibit a propensity to amalgamate, thereby forming electrically neutral composite defect clusters $\left[\left[Fe'_{Fe}-V^{\cdot\cdot}_O\right]^{\cdot}-\left[V'''_{Bi}-V^{\cdot\cdot}_O\right]'\right]^{\times}$. As x increases, the concentration of $\left[Fe'_{Fe}-V^{\cdot\cdot}_O\right]^{\cdot}$ gradually decreases, leading to a reduction in the number of such composite defect clusters and consequently diminishing their contribution to the internal electric field E_i. In the ceramics with 0 ≤ x ≤ 0.05, the concentrations of $\left[Fe'_{Fe}-V^{\cdot\cdot}_O\right]^{\cdot}$ and $[V'''_{Bi}-V^{\cdot\cdot}_O]'$ fall below the critical threshold necessary for forming electrically neutral composite defect clusters, resulting in

a consistently symmetrical form of the bipolar strain curve. These observations indicate that defect dipoles play a significant role in generating the internal electric field E_{i1} under Fe deficiency conditions, while their influence is suppressed in cases of Fe excess. In summary, it can be concluded that E_{i1} diminishes as x increases.

After polarization treatment, all ceramics exhibited asymmetric bipolar strain curves (Fig. 7(a)). In addition to the internal electric field E_{i1} contributed by defect dipoles, the polarization process induced a redistribution of space charge at the grain boundaries, resulting in an internal electric field E_{i2}. Both E_{i1} and E_{i2} work together to modulate the strain response. The value of E_{i2} is determined by the carrier concentration injected during polarization; the presence of oxygen vacancies introduces impurity energy levels, which are filled by the carriers injected during polarization, leading to a reduction in E_{i2}. In the ceramics with the lowest oxygen vacancy concentration at $x = 0$, E_{i2} is maximized after polarization, and the asymmetry of the bipolar strain curve is most pronounced. In the ceramics where $0 < x \leq 0.05$, the oxygen vacancy concentration is moderate, resulting in a weakened E_{i2} (Figs. 5(d) and 5(e)), and consequently, the asymmetry diminishes. Conversely, in the ceramics with the highest oxygen vacancy concentration at $-0.05 \leq x < 0$, E_{i2} is minimized, and the asymmetry of the post-polarization curve is dominated by E_{i1}. Figures 7(b) and 7(c) compare the relationship between the positive electric field strains S_{pos}^{+}, negative electric field strains S_{pos}^{-}, and the negative strain S_{neg} with respect to x before and after polarization. At electric field strengths of 40, 50, and 60 kV/cm, these strain parameters show consistent variation with x, indicating good reliability of the experimental results. In the unpolarized state, the ceramics at $x = -0.05$ exhibited the maximum strain values under a 60 kV/cm electric field, with S_{pos}^{+} at 0.29%, S_{pos}^{-} at 0.16%, and S_{neg} at 0.08%. As the internal electric field E_{i1} weakened, the strain values decreased. At $x = 0$, S_{pos}^{+}, S_{pos}^{-}, and S_{neg} dropped to 0.12%, 0.11%, and 0.03%, respectively, with further changes noted at $x = 0.05$: 0.12%, 0.12%, and 0.03%. The trend of the positive electric field strain S_{pos}^{+} in post-polarization ceramics aligns with the variation of the internal electric field E_i (Fig. 5(h)). The value of S_{pos}^{-} in the ceramics at $-0.05 \leq x < 0$ significantly decreased compared with the unpolarized state, which is attributed to defect pinning inhibiting electric domain switching. However, in the ceramics where $0 \leq x \leq 0.05$, S_{pos}^{-} notably increased alongside a significant negative strain S_{neg} due to the reduced pinning effect on electric domain switching and the enhancement of the internal bias field E_{i2}. The effective d_{33}^{*} of the ceramics in the range of $0 \leq x \leq 0.05$ was significantly improved under the influence of E_{i2} (Figs. 7(d1) and 7(d2)).

Figure 7(e) presents the unipolar strain curves of ceramics with three typical compositions, $x = -0.05$, 0, and 0.05, before and after polarization. Before polarization, as the internal electric field (E_{i1}) decreased, the strain values gradually declined from 0.5% for $x = -0.05$ to 0.13% and 0.12% for $x = 0$ and 0.05, respectively. After polarization, the unipolar strain of the $x = -0.05$ ceramics was significantly suppressed, decreasing by approximately 0.05%, while

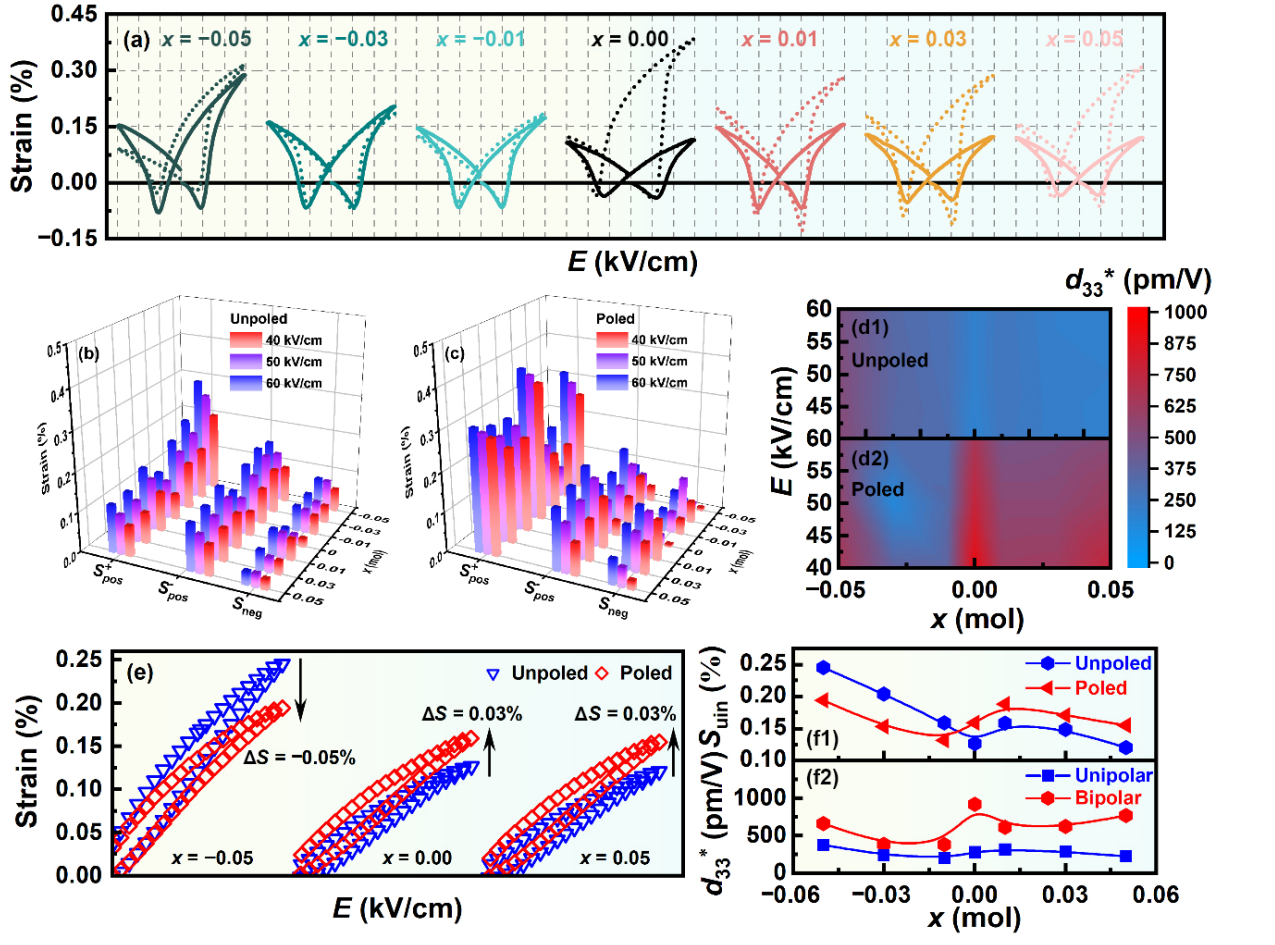

Fig. 7 (a) Strain evolution patterns of unpoled/poled BF_{1+x}–30BT piezoelectric ceramics under electric fields of 40, 50, and 60 kV/cm; (b, c) S_{pos}^{+}, S_{pos}^{-}, S_{neg}; (d1, d2) d_{33}^{*}; (e) three stages of unipolar S–E loops for BF_{1+x}–30BT piezoelectric ceramics at 60 kV/cm; (f1) unipolar strain before and after polarization at 60 kV/cm; (f2) unipolar and bipolar strains d_{33}^{*} at 40 kV/cm after polarization.

the unipolar strains of both the $x = 0$ and 0.05 ceramics increased by 0.03%.

Under the combined influence of space charge and defect dipoles, polarization had "opposing" regulatory effects on the unipolar strain behavior of ceramics within the ranges of $-0.05 \le x < 0$ and $0 \le x < 0.05$ (Fig. 7(f1)). The bipolar strain d_{33}^* was further enhanced post-polarization (Fig. 7(f2)), indicating that the increased domain wall motion under switching electric fields plays a crucial role in performance enhancement. At an electric field strength of 40 kV/cm, the highest unipolar d_{33}^* values were observed for the $x = -0.05$ and 0.01 ceramics, measuring 375 and 316 pm/V, respectively, while the $x = 0$ ceramics exhibited the maximum bipolar d_{33}^*, reaching 918 pm/V. In summary, the strain response of BF_{1+x}–30BT ceramics arises from the synergistic interaction among domain switching, the orientation/pinning effects of defect dipoles, and the distribution of space charge. The specific mechanisms involved require further in-depth investigation.

As illustrated in Fig. 8, the strain control mechanism in the BF_{1+x}–30BT ceramic system is evident. Prior to the process of polarization, the electric domains in all ceramics are randomly distributed, resulting in a macroscopic net polarization P_s of zero (Fig. 8(a1)). The application of an external electric field E_{ext} results in the initial alignment of the electric domains along the direction of the electric field, thereby inducing negative strain. With the subsequent increase in the electric field and the full realignment of the domains, electrostrictive strain is exhibited. The strains S_{pos}^+ and S_{pos}^- achieve their maximum levels at the point of maximum electric field (Figs. 8(a2) and 8(a3)). It has been demonstrated that upon elimination of the electric field, several domains undergo a process of reversion, thereby inducing a decline in strain. In consideration of the low defect concentration and the absence of internal bias fields E_{i1} and E_{i2} in the unpolarized ceramics, the values of S_{pos}^- are analogous to those of S_{pos}^+. This phenomenon results in the manifestation of a characteristic symmetric butterfly shape for the strain–electric field curve (Fig. 8(a4)). In ceramics with a high defect concentration ($-0.05 \le x \le 0$), the presence of oriented defect dipoles leads to an asymmetric S–E curve characteristic even prior to polarization (Fig. 8(c4)). The application of a positive E_{ext} enhances the S_{pos}^+ response

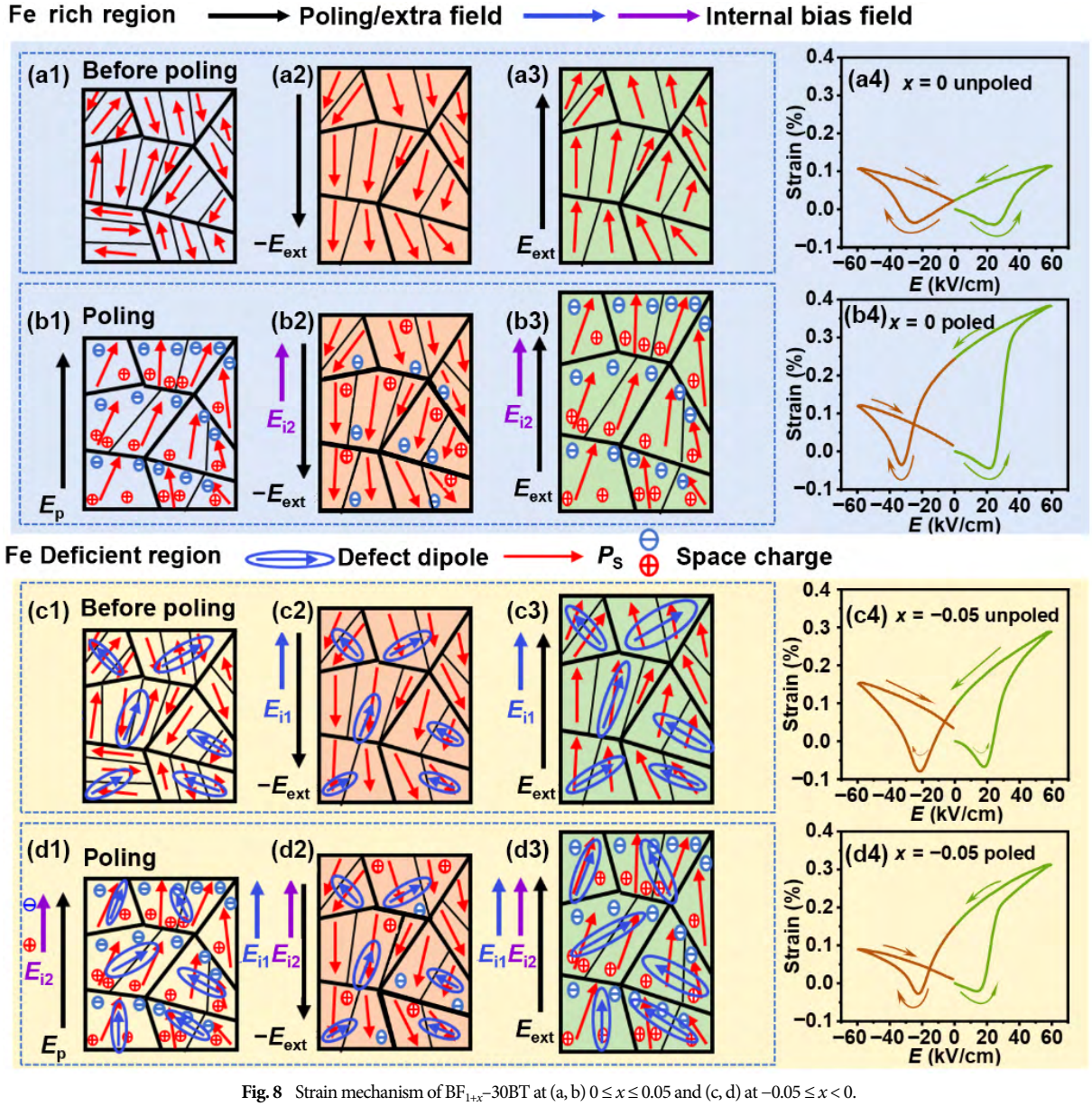

Fig. 8 Strain mechanism of BF_{1+x}–30BT at (a, b) $0 \le x \le 0.05$ and (c, d) at $-0.05 \le x < 0$.

(Fig. 8(c2)); conversely, E_{i1} weakens the effect of the negative electric field, while the pinning effect of the defect dipoles significantly suppresses S_{pos}^- (Fig. 8(c3)).

Following the process of polarization, the material's spontaneous polarization P_s exhibits a preferential alignment along the polarization direction. The injection of charges leads to the formation of space charge, thereby generating an internal bias field, E_{i2}. When the external electric field E_{ext} aligns with the direction of E_{i2}, domain switching is facilitated, thus enhancing the positive strain response S_{pos}^- (Fig. 8(b3)); conversely, when their directions oppose each other, the external field must first overcome the pinning effect of the internal bias field, leading to partial migration of the space charge. As the energy barrier for 180° domain switching is relatively high, the number of space charges migrating during this process is relatively small. This results in a weaker suppression of domain switching, which moderately increases the positive strain response S_{pos}^- under a negative electric field (Fig. 8(b2)). This asymmetric behavior, involving domain switching and charge migration, ultimately results in the formation of an asymmetric strain butterfly curve (Fig. 8(b4)). In the context of ceramics characterized by high defect concentrations, the internal bias field E_{i2}, generated by space charge, couples with the internal bias field E_{i1}, produced by defect dipoles (Figs. 8(d2) and 8(d3)). Consequently, the S–E curve remains asymmetrical post-polarization. However, the S_{pos}^- and unipolar strain S_{uni} are significantly reduced compared with the unpolarized state (Fig. 8(d4) and 7(e)). This reduction is attributed to the enhanced pinning effect of defect dipoles on the electric domains during the polarization process (Fig. 8(d1)), which promotes a highly ordered alignment of the electric domains along the direction of the external field. Consequently, the proportion of the intrinsic piezoelectric effect arising from lattice distortion increases, while the typically larger contributions from domain reorientation and domain wall motion, classified as extrinsic piezoelectric effects, are relatively diminished. It is important to note that the intrinsic contribution is generally less than the extrinsic contribution. Consequently, the overall strain capacity of the material post-polarization does not increase and may indeed decrease.

As demonstrated in Fig. 9, the PFM characterization of BF_{1+x}–30BT ceramics provides substantial evidence. The amplitude images (Fig. 9(b1)) demonstrate that the majority of the ceramic with x = 0 displays a distinct piezoelectric response, accompanied by significant amplitude signals. The results from domain writing experiments (Fig. S7 in the ESM) provide further confirmation of the effective reversal of electric domains within this ceramic. Furthermore, all ceramics display consistent domain structural characteristics, featuring both macroscopic domains and a limited number of island-like domains, corresponding to a coexisting state of R–PC phases [61] (Figs. 9(a2)–9(c2)). As x increases from −0.05 to 0.05, the number and density of island-like domains increase, attributed to the hindering effect of Fe_2O_3 on grain boundary migration during the sintering process, leading to a refinement of grain size and smaller domain dimensions. Until x = 0.05, the presence of a small number of microdomains and a substantial number of nanodomains is observed (Fig. 9(c2)). The ceramic with x = 0 possesses the best domain structure, and the formation of this multiscale domain structure enhances the

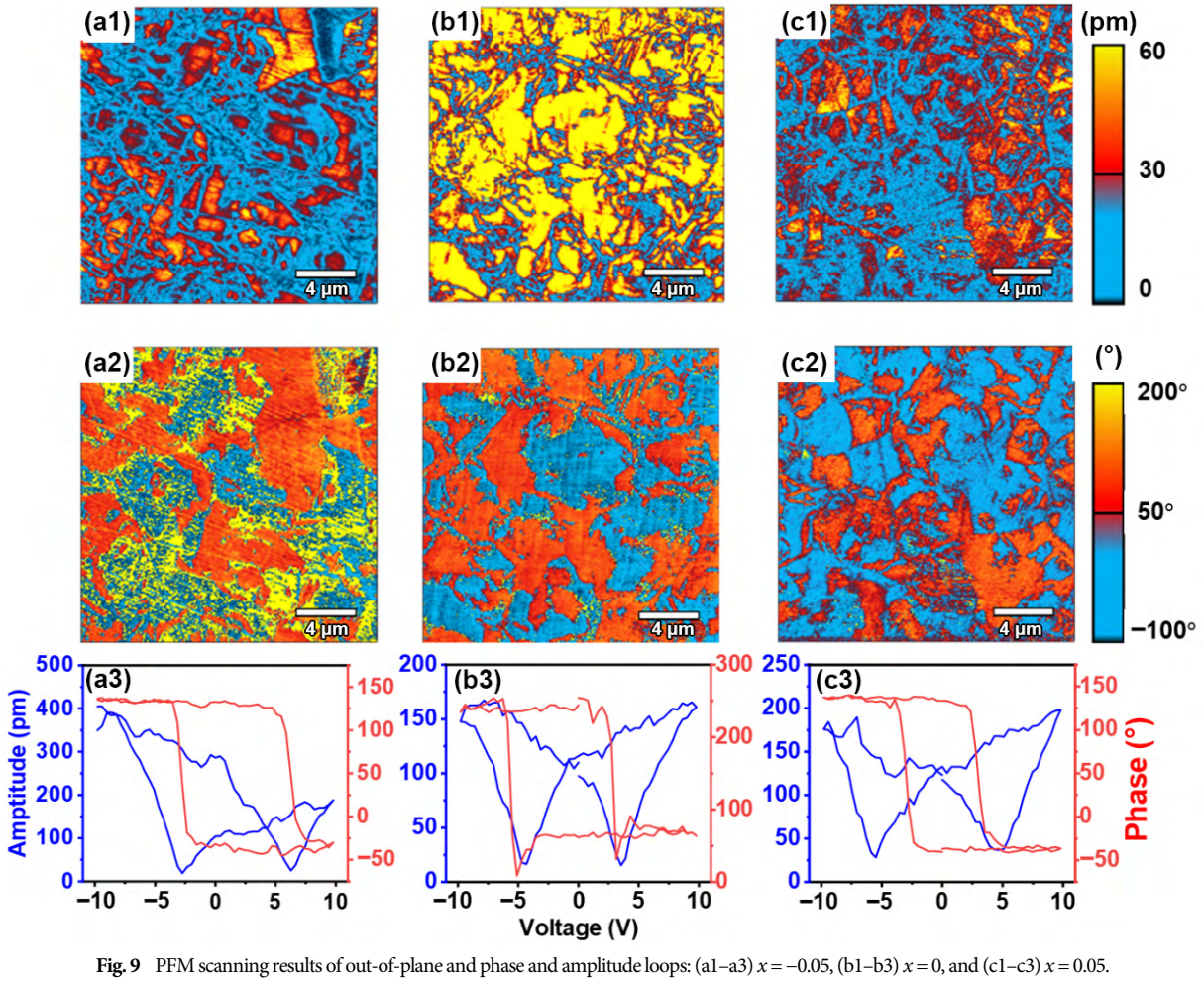

Fig. 9 PFM scanning results of out-of-plane and phase and amplitude loops: (a1–a3) x = −0.05, (b1–b3) x = 0, and (c1–c3) x = 0.05.

清華大学出版社 Tsinghua University Press | SciOpen

electromechanical strain performance of the polarized BF–BT ceramics.

It is noteworthy that in the ceramic with x = −0.05 (Fig. 9(a2)), an anomalous phase intensity signal is observed in the vicinity of the macroscopic domain walls. This phenomenon cannot be fully explained by conventional domain structures (71°, 90°, or 180° domains). It is hypothesized that this anomaly may be attributable to the pinning effect of defect dipoles aggregated at the domain walls. However, such strongly oriented dipole signals are not observed in ceramics with x = 0 and 0.05 (Figs. 9(b2) and 9(c2)). Further elucidation is furnished by SS-PFM analysis (Figs. 9(a3)–9(c3)). It is evident that all ceramics manifest typical 180° effective polarization switching behavior. The strain response is quantitatively characterized by amplitude curves, which reflect dynamic out-of-plane strain responses. The amplitude curve for x = −0.05 demonstrates a considerable degree of asymmetry, with strain values reaching approximately 400 pm. The maximum negative displacement (D_m^-) exceeds the positive displacement response (D_m^+), a phenomenon that may be attributed to an internal bias field E_{i2} induced by defect dipoles. For ceramics with x = 0 and 0.05, the symmetry of the amplitude curves progressively improves, with strain values decreasing to 250 and 220 pm, respectively, indicating a reduction in the contribution of defect dipoles to the strain response. This phenomenon aligns with the S–E curves exhibited by unpolarized BF_{1+x}–30BT ceramics.

Subsequently, the relationship between polarization intensity and strain versus electric field strength E (f = 1 Hz) for the ceramic with x = 0 was investigated across a temperature range of 25–125 °C. The results of these tests are presented in Figs. 10(a) and 10(b). As the temperature increases, the P–E loop approaches saturation. At room temperature and an electric field strength of 35 kV/cm, the optimal inverse piezoelectric coefficient (d_{33}^* = 1021 pm/V) was achieved. As the temperature increased, the optimal electric field strength corresponding to the peak in d_{33}^* shifted toward lower field strengths. At 100 °C, as the electric field strengthened, the maximum negative strain S_{neg} increased, while the positive strain S_{pos}^+ and remnant strain S_r diminished, indicating a more pronounced response from non-180° domain switching, contributing more significantly to strain. However, at high temperatures, such domain reorientations become difficult to maintain, leading to a reduction in strain. At a temperature of 125 °C and an electric field of 15 kV/cm, a substantial enhancement in d_{33}^* was observed, yielding a value of 1481 pm/V. As demonstrated in Fig. 10(d), the displacement (D) exhibits a linear decrease with increasing temperature, while d_{33}^* demonstrates an upward trend. As illustrated in Fig. 10(e), the *in situ* d_{33} value measured at 317.9 °C is 380.1 pC/N. These exceptional high-temperature properties indicate that this material is a highly promising candidate for next-generation high-temperature lead-free piezoelectric ceramics.

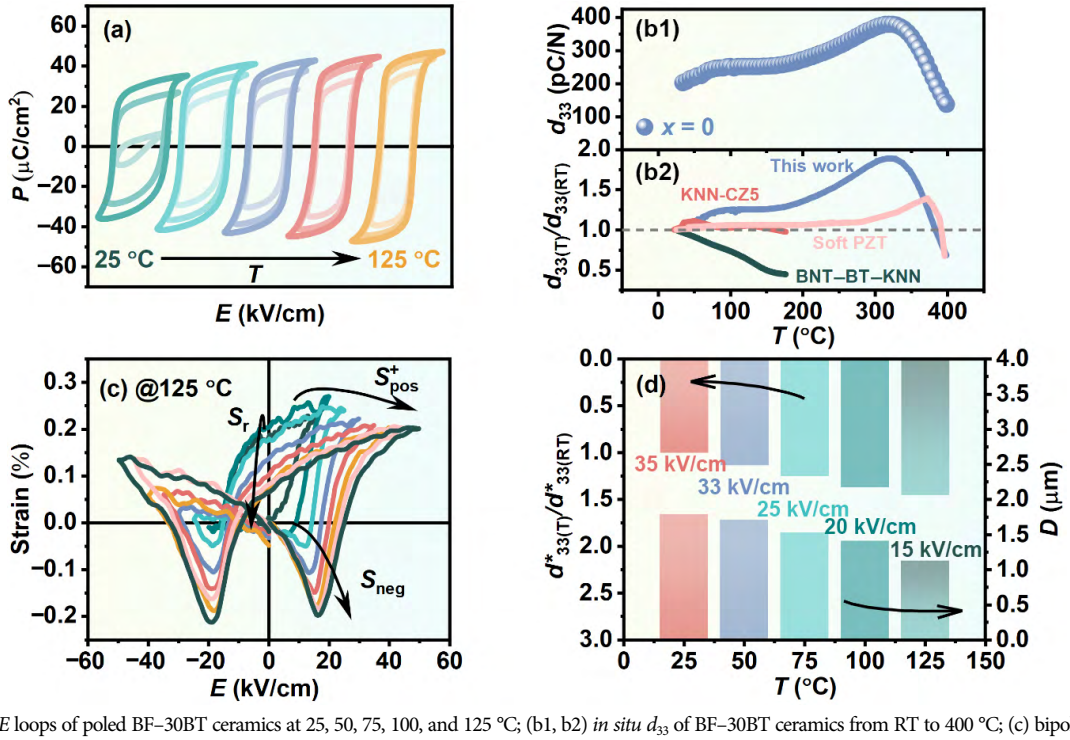

Fig. 10 (a) P–E loops of poled BF–30BT ceramics at 25, 50, 75, 100, and 125 °C; (b1, b2) *in situ* d_{33} of BF–30BT ceramics from RT to 400 °C; (c) bipolar S–E loops of poled BF–30BT (x = 0) ceramics at 100 °C; (d) $d_{33(T)}^*/d_{33(RT)}^*$ and displacement of BF–30BT ceramics at 25, 50, 75, 100, and 125 °C.

4 Conclusions

The one-step sintering process suppressed the formation of impurity phases such as $Bi_{25}FeO_{39}$ and $Bi_2Fe_4O_9$. $BiFe_{1+x}O_3$–$BaTiO_3$ ceramics achieved a high density and uniform microstructure across a wide composition range of $-0.05 \le x \le 0.05$. All ceramics exhibit stable C_R/C_{PC} ratios and a domain structure characterized by the coexistence of macroscopic domains and island domains within nanoscale domains. They demonstrate stable T_C = 488–503 °C and high d_{33} > 189 pC/N for $-0.05 \le x \le 0.03$. The d_{33} peak reached 214 pC/N. Significant Fe deficiency or excess doping revealed unique defect self-regulation behavior. As x increases, the activation energy for oxygen vacancy migration rises, strengthening the confinement of defect dipoles by oxygen vacancies, thereby suppressing high-temperature leakage conductance. Before polarization, excellent piezoelectric properties (d_{33}^* = 452 pm/V, d_{33} = 187 pC/N, and T_C = 489 °C) are exhibited at x = −0.05. After polarization treatment, the x = 0

ceramic achieved a large strain of 0.38% and comprehensive piezoelectric properties (d_{33}^* = 1021 pm/V, d_{33} = 201 pC/N, and T_C = 503 °C). The material exhibits good high-temperature strain performance, maintaining a high d_{33}^* of 1481 pm/V under an electric field of 15 kV/cm at 125 °C. This demonstrates its potential as an ideal candidate material for next-generation high-temperature lead-free piezoelectric devices.

Acknowledgements

This work was supported by the Basic Science Center Project of the National Natural Science Foundation of China (No. 52388201), the National Natural Science Foundation of China (No. 52302211), and the Fundamental Research Funds for the Central Universities (No. FRF-TP-24-005A).

Availability of data and materials

The data that support the findings of this study are available from the corresponding author upon reasonable request.

Competing interests

The authors have no competing interests to declare that are relevant to the content of this article.

Electronic Supplementary Material

Supplementary material is available in the online version of this article at https://doi.org/10.26599/JAC.2026.9221302.

References

[1] Narayan B, Malhotra JS, Pandey R, *et al.* Electrostrain in excess of 1% in polycrystalline piezoelectrics. *Nat Mater* 2018, **17**: 427–431.
[2] Hao JG, Li W, Zhai JW, *et al.* Progress in high-strain perovskite piezoelectric ceramics. *Mat Sci Eng* 2019, **135**: 1–57.
[3] Lu ZL, Wang G, Bao WC, *et al.* Superior energy density through tailored dopant strategies in multilayer ceramic capacitors. *Energ Environ Sci* 2020, **13**: 2938–2948.
[4] Wang G, Fan ZM, Murakami S, *et al.* Origin of the large electrostrain in $BiFeO_3$–$BaTiO_3$ based lead-free ceramics. *J Mater Chem A* 2019, **7**: 21254–21263.
[5] Wang B, Liu W, Zhao TL, *et al.* Promising lead-free $BiFeO_3$–$BaTiO_3$ ferroelectric ceramics: Optimization strategies and diverse device applications. *Prog Mater Sci* 2024, **146**: 101333.
[6] Zhang MH, Zhang QH, Yu TT, *et al.* Enhanced electric-field-induced strains in (K,Na)NbO_3 piezoelectrics from heterogeneous structures. *Mater Today* 2021, **46**: 44–53.
[7] Lee MH, Kim DJ, Park JS, *et al.* High-performance lead-free piezoceramics with high curie temperatures. *Adv Mater* 2015, **27**: 6976–6982.
[8] Wu JG, Fan Z, Xiao DQ, *et al.* Multiferroic bismuth ferrite-based materials for multifunctional applications: Ceramic bulks, thin films and nanostructures. *Prog Mater Sci* 2016, **84**: 335–402.
[9] Selbach SM, Einarsrud MA, Grande T. On the thermodynamic stability of $BiFeO_3$. *Chem Mater* 2009, **21**: 169–173.
[10] Li F, Lin DB, Chen ZB, *et al.* Ultrahigh piezoelectricity in ferroelectric ceramics by design. *Nat Mater* 2018, **17**: 349–354.
[11] Kim S, Miyauchi R, Sato Y, *et al.* Piezoelectric actuation mechanism involving extrinsic nanodomain dynamics in lead-free piezoelectrics. *Adv Mater* 2023, **35**: 2208717.
[12] Li F, Wang B, Gao XY, *et al.* Ferroelectric materials toward next-generation electromechanical technologies. *Science* 2025, **389**: eadn4926.
[13] Zhu LF, Liu D, Shi XM, *et al.* Ultrahigh piezoelectric performances of (K,Na)NbO_3 based ceramics enabled by structural flexibility and grain orientation. *Nat Commun* 2025, **16**: 901.
[14] Huangfu G, Zeng K, Wang BQ, *et al.* Giant electric field-induced strain in lead-free piezoceramics. *Science* 2022, **378**: 1125–1130.
[15] Lin JM, Lv F, Hong ZJ, *et al.* Ultrahigh piezoelectric response obtained by artificially generating a large internal bias field in $BiFeO_3$–$BaTiO_3$ lead-free ceramics. *Adv Funct Mater* 2024, **34**: 2313879.
[16] Xi KB, Guo JZ, Zheng MP, *et al.* Defect engineering with rational dopants modulation for high-temperature energy harvesting in lead-free piezoceramics. *Nano-Micro Lett* 2025, **17**: 55.
[17] Lee MH, Choi HI, Kim DJ, *et al.* Hard piezoelectric properties of $MnCO_3$-doped lead-free $BiFeO_3$–$BaTiO_3$ ceramics with high curie temperature. *ACS Appl Mater Inter* 2025, **17**: 29570–29582.
[18] Huang YT, Qian J, Lin JM, *et al.* Space charge–electron transmission for enhancing high-temperature piezoelectricity in BF-based ceramics. *Adv Funct Mater* 2026, **36**: 11290.
[19] Liu H, Hao YJ, Yang ZQ, *et al.* Exceptional electrostrain with minimal hysteresis and superior temperature stability under low electric field in KNN-based lead-free piezoceramics. *J Adv Ceram* 2024, **13**: 364–372.
[20] Lin JM, Guo XW, Liu B, *et al.* Exceptionally large thickness-independent longitudinal strain in lead-free piezoceramics via defect dipole engineering. *Adv Funct Mater* 2026, **36**: 22553.
[21] Dho J, Qi X, Kim H, *et al.* Large electric polarization and exchange bias in multiferroic $BiFeO_3$. *Adv Mater* 2006, **18**: 1445–1448.
[22] Tsurumaki A, Yamada H, Sawa A. Impact of Bi deficiencies on ferroelectric resistive switching characteristics observed at p-type Schottky-like Pt/$Bi_{1-\delta}FeO_3$ interfaces. *Adv Funct Mater* 2012, **22**: 1040–1047.
[23] Meng K, Li W, Tang X-G, *et al.* A Review of a Good Binary Ferroelectric Ceramic: $BiFeO_3$–$BaTiO_3$. *ACS Appl Electron Mater* 2022, **4**: 2109–2145.
[24] Peng XY, Tang YC, Zhang BP, *et al.* High Curie temperature $BiFeO_3$–$BaTiO_3$ lead-free piezoelectric ceramics: Ga^{3+} doping and enhanced insulation properties. *J Appl Phys* 2021, **130**: 144104.
[25] Qi YG, Xia BJ, Guo XX, *et al.* Enhanced magnetoelectric response in Sc-doped $BiFeO_3$–$BaTiO_3$ ceramics. *Ceram Int* 2024, **50**: 52514–52523.
[26] Zhou XX, Tang YC, Li HZ, *et al.* $BiAlO_3$-modified $BiFeO_3$–$BaTiO_3$ high Curie temperature lead-free piezoelectric ceramics with enhanced performance. *Rare Metals* 2023, **42**: 3839–3850.
[27] Wan Y, Li Y, Li Q, *et al.* Microstructure, ferroelectric, piezoelectric, and ferromagnetic properties of Sc-modified $BiFeO_3$–$BaTiO_3$ multiferroic ceramics with MnO_2 addition. *J Am Ceram Soc* 2014, **97**: 1809–1818.
[28] Liu XH, Xu Z, Wei XY, *et al.* Ferroelectric and ferromagnetic properties of 0.7$BiFe_{1-x}Cr_xO_3$–0.3$BaTiO_3$ solid solutions. *J Am Ceram Soc* 2008, **91**: 3731–3734.
[29] Sun YY, Yang HB, Guan SB, *et al.* Strong piezoelectricity of Li_2CO_3-doped $BiFeO_3$–$BaTiO_3$–$Bi(Zn_{0.5}Ti_{0.5})O_3$ lead-free piezoelectric ceramics with high Curie temperature and high temperature stability. *J Alloy Compd* 2020, **819**: 153058.
[30] Guan SB, Yang HB, Zhao YZ, *et al.* Effect of Li_2CO_3 addition in $BiFeO_3$–$BaTiO_3$ ceramics on the sintering temperature, electrical properties and phase transition. *J Alloy Compd* 2018, **735**: 386–393.
[31] Yang JC, Huang MM, Wang FF, *et al.* Low temperature sintering, structure and electrical properties of $BiFeO_3$–$BaTiO_3$ based piezoelectric ceramics using CuO–B_2O_3 composite sintering aids. *Mater Sci Eng B—Adv* 2023, **298**: 116872.
[32] Yang HB, Zhou CR, Liu XY, *et al.* Piezoelectric properties and temperature stabilities of Mn- and Cu-modified $BiFeO_3$–$BaTiO_3$ high temperature ceramics. *J Eur Ceram Soc* 2013, **33**: 1177–1183.
[33] Tang YC, Yin Y, Song AZ, *et al.* Boosting the high performance of $BiFeO_3$–$BaTiO_3$ lead-free piezoelectric ceramics: One-step preparation and reaction mechanisms. *ACS Appl Mater Inter* 2022, **14**: 30991–30999.
[34] Tang YC, Yin Y, Song AZ, *et al.* High-performance $BiFeO_3$–$BaTiO_3$ lead-free piezoceramics insensitive to off-stoichiometry and processing temperature. *J Materiomics* 2023, **9**: 353–361.
[35] Ali Khan S, Ahmed T, Park HW, *et al.* Effects of B- and A/B-sites

Codoping on lattice distortion and defect concentration for high electromechanical response of lead-free piezoelectrics. *Acta Mater* 2024, **278**: 120262.
[36] Alrobei H, Habib M, Ali S, *et al.* Enhanced electromechanical performance of Si-modified lead-free $BiFeO_3$–$BaTiO_3$ ceramics for high-temperature piezoelectric applications. *PLoS One* 2025, **20**: e0318768.
[37] Habib M, Tang L, Xue GL, *et al.* Design and development of a new lead-free $BiFeO_3$–$BaTiO_3$ quenched ceramics for high piezoelectric strain performance. *Chem Eng J* 2023, **473**: 145387.
[38] Liu X, Zhai JW, Shen B. Novel bismuth ferrite-based lead-free incipient piezoceramics with high electromechanical response. *J Mater Chem C* 2019, **7**: 5122–5130.
[39] Wang L, Liang RH, Zhou ZY, *et al.* High electrostrain with high Curie temperature in $BiFeO_3$–$BaTiO_3$-based ceramics. *Scripta Mater* 2019, **164**: 62–65.
[40] Yuan HB, Li LL, Hong H, *et al.* Low sintering temperature, large strain and reduced strain hysteresis of $BiFeO_3$–$BaTiO_3$ ceramics for piezoelectric multilayer actuator applications. *Ceram Int* 2021, **47**: 31349–31356.
[41] Habib M, Ahmad P, Akram F, *et al.* High and temperature-insensitive piezoelectric performance in the lead-free Sm-doped $BiFeO_3$–$BaTiO_3$ ceramics with high Curie temperature. *Ceram Int* 2022, **48**: 26608–26617.
[42] Chen JG, Daniels JE, Jian J, *et al.* Origin of large electric-field-induced strain in pseudo-cubic $BiFeO_3$–$BaTiO_3$ ceramics. *Acta Mater* 2020, **197**: 1–9.
[43] Habib M, Lee MH, Kim DJ, *et al.* Phase diagram for Bi-site La-doped $BiFeO_3$–$BaTiO_3$ lead-free piezoelectric ceramics. *J Materiomics* 2021, **7**: 40–50.
[44] Li P, Zhai JW, Shen B, *et al.* Ultrahigh piezoelectric properties in textured (K,Na)NbO_3-based lead-free ceramics. *Adv Mater* 2018, **30**: 1705171.
[45] Wang K, Yao FZ, Jo W, *et al.* Temperature-insensitive (K,Na)NbO_3-based lead-free piezoactuator ceramics. *Adv Funct Mater* 2013, **23**: 4079–4086.
[46] Saito Y, Takao H, Tani T, *et al.* Lead-free piezoceramics. *Nature* 2004, **432**: 84–87.
[47] Cen ZY, Huan Y, Feng W, *et al.* A high temperature stable piezoelectric strain of KNN-based ceramics. *J Mater Chem A* 2018, **6**: 19967–19973.
[48] Zheng T, Wu HJ, Yuan Y, *et al.* The structural origin of enhanced piezoelectric performance and stability in lead free ceramics. *Energ Environ Sci* 2017, **10**: 528–537.
[49] Hua Y, Qian J, Yang YX, *et al.* Broad temperature plateau for high piezoelectric coefficient by embedding PNRs in singe-phase KNN-based ceramics. *Adv Funct Mater* 2025, **35**: 2414348.
[50] Wang DW, Khesro A, Murakami S, *et al.* Temperature dependent, large electromechanical strain in Nd-doped $BiFeO_3$–$BaTiO_3$ lead-free ceramics. *J Eur Ceram Soc* 2017, **37**: 1857–1860.
[51] Li TY, Liu C, Shi P, *et al.* High-performance strain of lead-free relaxor-ferroelectric piezoceramics by the morphotropic phase boundary modification. *Adv Funct Mater* 2022, **32**: 2202307.
[52] Chen PY, Chen CS, Tu CS, *et al.* Large E-field induced strain and polar evolution in lead-free Zr-doped 92.5%($Bi_{0.5}Na_{0.5}$)TiO_3–7.5%$BaTiO_3$ ceramics. *J Eur Ceram Soc* 2014, **34**: 4223–4233.
[53] Tai DQ, Li B, Xue HY, *et al.* $BiFeO_3$–$BaTiO_3$ ferroelectrics: Decrypting the mechanism of rare earth doping-induced electrical property discrepancy via scaling behavior and multi-level structure. *Acta Mater* 2024, **262**: 119411.
[54] Habib M, Zhou XF, Tang L, *et al.* Phase and domain engineering strategy for enhancement of piezoelectricity in the lead-free $BiFeO_3$–$BaTiO_3$ ceramics. *J Materiomics* 2023, **9**: 920–929.
[55] Prateek, Thakur VK, Gupta RK. Recent progress on ferroelectric polymer-based nanocomposites for high energy density capacitors: Synthesis, dielectric properties, and future aspects. *Chem Rev* 2016, **116**: 4260–4317.
[56] Li Q, Zhang MH, Zhu ZX, *et al.* Poling engineering of (K,Na)NbO_3-based lead-free piezoceramics with orthorhombic–tetragonal coexisting phases. *J Mater Chem C* 2017, **5**: 549–556.
[57] Fan ZH, Dai J, Huang YY, *et al.* Superior energy storage capacity of polymer-based bilayer composites by introducing 2D ferroelectric micro-sheets. *Nat Commun* 2025, **16**: 1180.
[58] Xue MP, Tang YC, Shan ZH, *et al.* Deciphering the leakage conduction mechanism of $BiFeO_3$–$BaTiO_3$ lead-free piezoelectric ceramics. *J Adv Ceram* 2023, **12**: 1844–1856.
[59] Li JL, Qu WB, Daniels J, *et al.* Lead zirconate titanate ceramics with aligned crystallite grains. *Science* 2023, **380**: 87–93.
[60] Huangfu G, Wang J, Zhang HM, *et al.* Deciphering the effect of defect dipoles on the polarization and electrostrain behavior in perovskite ferroelectrics. *Nano Lett* 2024, **24**: 12148–12155.
[61] Li CY, Zheng T, Wu JG. Competitive mechanism of temperature-dependent electrical properties in $BiFeO_3$–$BaTiO_3$ ferroelectrics controlled by domain evolution. *Acta Mater* 2021, **206**: 116601.